MULTI-SEGMENT PHOTOVOLTAIC LASER POWER CONVERTERS AND THEIR ELECTRICAL LOSSES

Rok Kimovec[1], Henning Helmers[2], Andreas W. Bett[2], Marko Topič[1]

[1]University of Ljubljana, Faculty of Electrical Engineering, Tržaška cesta 25, 1000 Ljubljana, Slovenia
Tel: +386 1 4768 276, Fax: +386 1 4768 276, E-mail: rok.kimovec@fe.uni-lj.si
[2] Fraunhofer Institute for Solar Energy Systems ISE, Heidenhofstraße 2, 79110 Freiburg, Germany

ABSTRACT: The electrical power losses of small area six-segment monolithic interconnected GaAs laser power converter are analyzed based on a variety of measurements and an experimentally validated numerical 2.5-dimensional distributed electrical model. Input parameters for the developed model were extracted from a wide-range of independent measurements performed on the manufactured devices. The complex geometry of the device is implemented in the model with digital images of photolithographic masks. Validity of the built model is confirmed by a good agreement between measured and simulated spatial electroluminescence response and a good agreement between measured and simulated dark and illuminated *J-V* curves is observed. It is shown that distributed ohmic losses limit the efficiency of the studied device above the optimal ($G_{optimal}$=13.2 W/cm^2) monochromatic irradiance (λ_0=809 nm). At high irradiance (G_{high}=83.1 W/cm^2), the photovoltaic conversion efficiency is decreased by 17%$_{abs.}$, due to combined ohmic losses, where more than 88%$_{rel.}$ of the losses are caused by Joule heating in the lateral conduction layer (which is specific to this kind of multi-segment device). Below the optimal irradiance, minority carrier recombination at the perimeter of the *pn*-junction is identified as the limiting factor. At G_{low}=1.8 W/cm^2 perimeter recombination causes 5.5%$_{abs.}$ decrease of the conversion efficiency. Additionally, photo-induced conductivity in the semi-insulating GaAs substrate leads to a leakage current between adjacent segments which reduces the efficiency for all studied irradiances equally by 1.2%$_{abs}$.

Keywords: photovoltaics, monolithic interconnection, gallium arsenide based cells, III-V semiconductors, simulation, distributed model, electroluminescence, electrical losses, power-over-fiber, power-by-light

1 INTRODUCTION

Laser Power Converters (LPC) [1–3] are photovoltaic (PV) devices converting monochromatic light into electrical energy typically used in a "power-over-fiber" (alternatively "power-by-light") electrical power supplies [4–6]. Utilizing a nonconductive energy transmission medium, (usually a multi-mode optical fiber) such power supply systems are inherently immune to electromagnetic radiation and provide a galvanic isolation between the power source and powered electronic circuits or devices.

The output voltage of a single-junction single-segment LPC made of GaAs in the maximum power point is around 1 V [7]. Since this voltage is often too low to power electronic devices directly, multi-segment LPCs are used to increase the output voltage of the PV device (also known as monolithic interconnected modules or MIMs) [2, 8]. In a multi-segment LPC, one vertical *pn*-junction is grown on a semi-insulating substrate and a wet chemical treatment is then applied to electrically separate individual segments directly on the chip. Thus, a galvanic and spatial separation of the *pn*-junctions is achieved. With the means of series interconnections of adjacent segments, a mini-module with an output voltage around N_{seg}*1V is realized, where N_{seg} is the number of segments [9].

In this work we present a detailed electrical power loss analysis of a six-segment monolithically interconnected GaAs laser power converter based on an experimentally validated electrical distributed model. The majority of the input parameters for the model were extracted from independent measurements performed on the manufactured device. Furthermore, digital images of photolithographic masks were used to maintain exact geometrical features of the multi-segment LPC. Measured and simulated illuminated and dark *J-V* curves are in good agreement, showing us that developed model is able to reproduce the measured data. To ensure the validity of the model, we used completely independent

characteristic of the device presented by measured and simulated electroluminescence images. With the validated model we investigate and quantify the contribution of various electrical loss mechanisms (i.e. Joule heating, recombination and shunt losses) to overall electrical power losses in the manufactured device.

2 SPECIMEN DESCRIPTION

In this work we study and present electrical loss mechanisms in a small area radial pie-shaped six-segment monolithic interconnected GaAs laser power converter manufactured at Fraunhofer ISE. A picture of the device is shown in Figure 1. The diameter of the circular area measured between the busbars is 2.08 mm, resulting in an inner device area of 3.39 mm^2. In the studied device, 11.1% of the area of an individual segment (0.63 mm^2) is covered with a cathode busbar and additionally 7.2% is covered by metal front grid. This metal coverage results in a segment active area of approximately 0.52 mm^2 exposed to the impinging light.
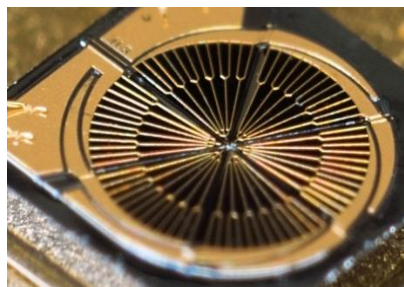
FIGURE 1: A macro photograph of the six-segment GaAs MIM LPC investigated in this work. Radius of inner circular area between the busbars is *R*=1.04 mm.

The epitaxial structure, shown in Figure 2, was grown by metalorganic vapor phase epitaxy (MOVPE) on a 4" semi-insulating (S.I.) GaAs substrate and is based on a GaAs *np*-junction (3650 nm thick absorber). On top of

the *np*-junction is a 400 nm thick *n*-type GaInP window layer (FSF) [10] which is transparent for the monochromatic light and reinforces lateral current flow between grid fingers. Below the *np*-junction is a *p*-type GaInP back surface field (BSF). A highly doped 5 µm thick *n*-type GaAs lateral conduction layer (LCL) is used for lateral interconnection of the individual PV cell segments. A tunnel diode provides ohmic connection between the *p*-type BSF and the *n*-type LCL. A highly doped *n*-type GaAs cap layer above the window provides a low-ohmic front side metal-semiconductor contact. After the MOVPE growth of the structure devices on the wafer are fabricated with standard micro-structuring photolithographic processes, wet etching, polyimide insulation, metal evaporation and a two layer anti-reflection (AR) coating [11]. Further details on the device structure and processing can be found elsewhere [2, 12].
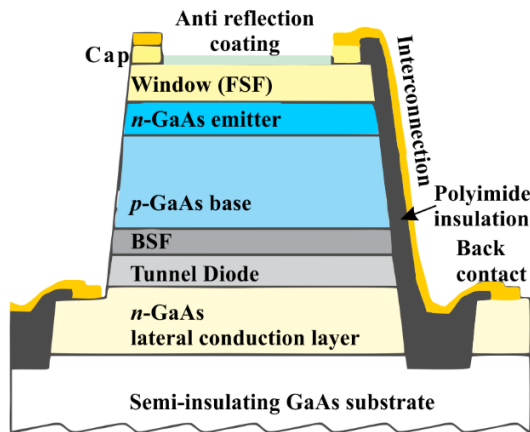

FIGURE 2: A conceptual cross-section of the investigated device. (not to scale)

3 NUMERICAL DISTRIBUTED MODEL OF SIX-SEGMENT GaAs MIM LPC

A complex geometry and epitaxial structure result in a complex current flow in the investigated MIM device. Therefore, a distributed numerical model based on a real device structure is required to accurately simulate electrical losses. In this section, we provide basic description of the investigated six-segment GaAs MIM LPC model implemented in two and a half dimensional (2.5D) PV simulation tool PVMOS [13]. It should be pointed out that most of the electrical input parameters for the model were extracted from a variety of measurements performed on the manufactured device, as described in the next section, and remaining few were obtained from literature [12]. Such modeling approach enables us to implement a stack of two dimensional simulation electrodes, where each electrode represents a specific device layer, described by realistic electrical parameters. Planar electrodes are vertically interconnected with each other with so called elementary units, to form a geometrically accurate three dimensional electrical representation of the device.

The used modeling approach mimics the manufacturing procedures, i.e. the MOVPE growth, micro-structuring, polyimide insulation, and metal evaporation as described above. First we defined a stack of four resistive simulation electrodes, where each simulation electrode presents the sheet resistances of the modeled layer (i.e. S.I.-substrate, LCL + base,

emitter + window and metallization). Between the nodes of the electrodes, vertical connections were established with elementary units. The role of the elementary units depends on its position in the device; standard two diode electrical PV model describe the bulk photoactive region, whereas simple resistive elementary units describe the rest of the device. The resistance of each resistive elementary unit is set to the appropriate value, based on its position in the device.

Afterwards the definition of geometrical features of the device is set. In the areas, defined by the digital images of photolithographic masks, the properties of simulation electrodes and elementary units were changed to represent the role of the explicit area in the device. For example, mesa etch sheet resistances in mesa etch regions were set to high values and all elementary units in these regions were set to high resistances to suppress the simulated current flow in those regions. Further, to model the photo-induced conductivity in the S.I.-substrate [12, 14], its sheet resistance was lowered at the isolation trenches where the substrate is exposed to incident light. Increased minority carriers recombination were specifically implemented at the perimeter of the *pn*-junctions by increasing the dark saturation current of the second diode J_{02} in the two diode PV model of the photo active area [12].

In similar manner, all specific device features were taken into account and implemented accurately. Further details and explanations can be found in Ref. [12].

4 PARAMETRIZATION OF THE SPECIMEN

A variety of measurements was performed on the investigated specimen to evaluate the device performance and extract electrical parameters of individual device features.

First a dark current-voltage (*I-V*) curve and a series of illuminated *I-V* curves were measured at constant temperature *T*=25 °C. The dark *I-V* curve, measured with a precision source-measurement unit, was divided by segment area to obtain the dark current density-voltage (*J-V*) curve. From this curve, in reverse polarity bias, we extracted the area-weighted shunt resistance. This value presents a *pn*-junction shunting and was accordingly modeled as a parallel conductance in two-diode electrical PV model of the active area. Additionally, the combined (i.e. depletion region and perimeter recombination) dark saturation current density for the second diode in two diode PV model (J_{02}) was extracted from the dark *J-V* curve. Bulk component J_{02B} (depletion region) of the combined J_{02} was obtained from literature [15] and the perimeter J_{02P} component was obtained from following equation:

$$J_{02} = J_{02b} + \frac{P}{A} \cdot J_{02p},$$

where perimeter to area ratio (*P/A*) of the investigated device is 57 cm^{-1}.

Illuminated *I-V* curves were measured under transient monochromatic (λ_0=809 nm) illumination at various irradiances *G*, utilizing a four probe measurement technique [16]. Again, measured *I-V* curves were divided by segment area to obtain *J-V* curves, from which current density-open circuit voltage (J_{SC}-V_{OC}) pairs were extracted. These pairs were further used to obtain saturation current density for the first diode (J_{01}) in two diode PV model (neutral region recombinations). Ideality factors (*n*), for the two diode electrical PV model, were

preset to 1 and 2 for J_{01} and J_{02B}, J_{02P} respectively.

Furthermore, sheet resistances of individual epitaxial layers were measured with a transmission line method (TLM) [17] on the same wafer as the manufactured device. The same method was used to measure the specific metal-semiconductor contact resistance at the cap layer (front contact) as well as at the lateral conduction layer (back contact). Also the sheet resistance of metallization was measured on the test structure, manufactured on the same wafer. The area weighted resistance for vertical current flow through the structure was calculated from nominal doping levels and layers thicknesses and literature values for mobility of majority carriers [18].

Electrical parameters of the semi-insulating substrate were obtained independently. The sheet resistance of the substrate in the dark was calculated from nominal thickness and literature resistivity [19]. Additionally, illuminated sheet resistance of the substrate was obtained iteratively, for each irradiance separately, by fitting the modeled slope of the *J-V* curve at J_{SC} to the measured slope of the *J-V* curve again at J_{SC}.

With described procedures a full set of electrical parameters, used as input parameters for the model, was obtained. For quantitative values and details see [12].

4 VALIDITY OF THE MODEL

The complexity of the device results in a complex numerical model. Comparison of the measured and simulated dark and illuminated *J-V* curves as seen in Figure 3 were used to confirm that the established model is able to reproduce the device behavior. An illuminated *J-V* curve presented in this plot was obtained under monochromatic (λ_0=809 nm) irradiance *G*=4.4 W/cm^2. At this irradiance very good agreement between simulation and measurement is observed. For higher irradiance slight underestimation of ohmic losses in our model is presented [12], which is also observed in the dark *J–V* curve at high voltages (>7 V); voltage region where the device is limited by series resistance losses.
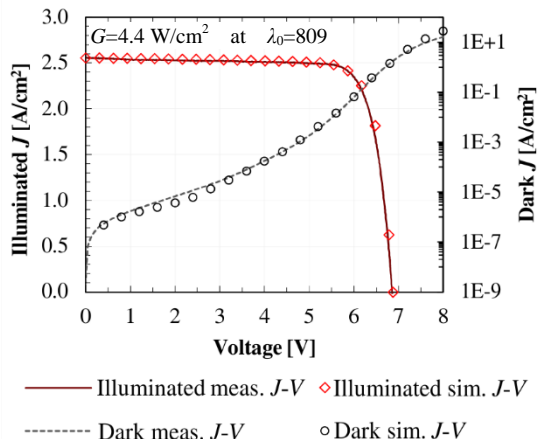
FIGURE 3: Simulated (symbols) and measured (lines) illuminated and dark *J-V* curves of the six-segment MIM GaAs LPC.

The good agreement between measured and simulated *J-V* curves is not sufficient to confirm the validity of the model, since various sets of input parameters of such complex model, could result in similar simulated *J-V* characteristics. Also, some of the

input parameters were extracted from the same measured *J-V* curves, and therefore good agreement between the measurements and simulations is anticipated. To really validate the model, good agreement between simulation and measurement for an independent characteristic of the device, which has not been used for the parametrization, must be established. For that purpose, we used measured and simulated electroluminescence (EL) images. Very good agreement between the measured and simulated normalized EL, as plotted in Figure 4, ensure us that our model well represents the device in detail, is able to predict its behavior, and consequently can be used to study different loss mechanisms in the specimen.
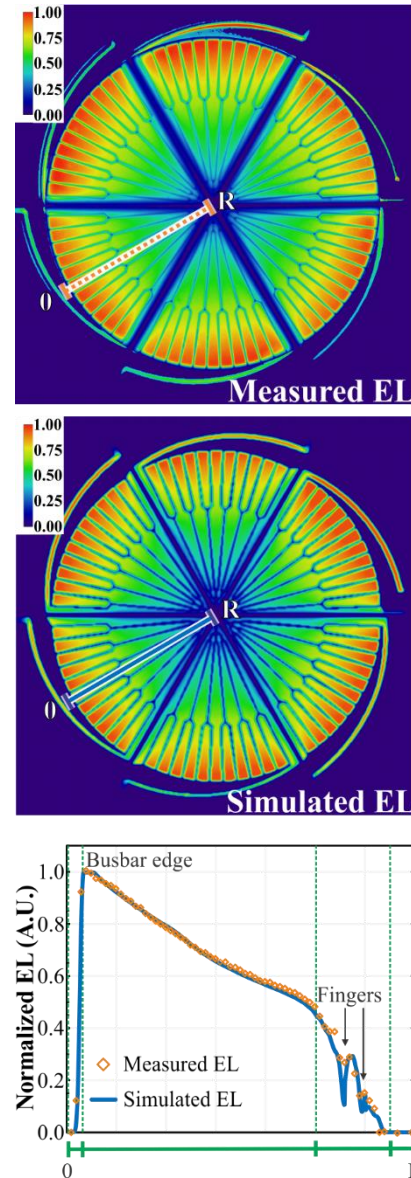
FIGURE 4: Top: Measured normalized EL image of the six-segment MIM LPC at I_{bias}=10mA. Higher values on the color scale present higher EL emission. Middle: Simulated normalized EL image of the six-segment MIM LPC at I_{bias}=10mA. Bottom: Line scans from the edge towards center as marked with the lines in the EL images. Further explanations are given in the text.

The measured EL image was obtained with a scientific CCD camera, fitted with a microscope objective, at forward current bias I_{bias}=10 mA (V_{bias}≈6.8 V) and at

controlled temperature T=25 °C [20]. Dark background was subtracted from the raw EL image and then the image was normalized to the maximum value. The simulated EL image was obtained from the simulated spatial map of the junction voltage V_j (at I_{bias}=10 mA, V_{bias}≈6.8 V, T=25 °C) as [21]:

$$EL = const. \cdot \exp\left(\frac{q \cdot V_j}{k \cdot n_{EL} \cdot T} - 1\right),$$

where kT/q is the thermal voltage, and n_{EL}=2 was obtained from the measured $EL(V_{bias})$ slope.

Investigation of the spatial EL data and a representative line scan (bottom of Figure 4) from the edge (0) towards the center (R) reveal operating characteristics of the studied device. At the origin of the line scan, EL emission from the device is completely blocked by the busbar metallization. Further towards the center of the specimen, the negative slope of the EL signal originates from the voltage drop related to the lateral flow of the injected current through semiconductor layers. Primarily, the EL emission drop is caused by the current flow through LCL; thus, the drop increases with increasing distance from the rear contact. In this region, two slopes of the EL signal drop can be observed. The transition of the slopes occurs where two grid fingers merge into one; indicating that the drop of the junction voltage is not caused only by the LCL, but also by the lateral current flow in the finger grid and window layer. At the edges of the *pn*-junctions the EL emission severely drops because of the increased recombination at the perimeter. In the line scan this is observed as the pronounced drop of the EL signal at the center, while distinct dips in the EL emission relate to the metal fingers.

5   RESULTS AND DISCUSION

The major electrical losses in MIM LPC are caused by three distinct loss mechanisms.

- Inherently long distances for the lateral current flow through the structure with a finite conductance results in a severe ohmic losses related Joule heating. This effect is severely pronounced in the lateral conduction layer, where no metallization is present to provide very low ohmic lateral current path and all photo generated current must flow through this semiconductor layer.
- Small area and segmentations of the specimen results in a large perimeter to area ratio. Due to imperfections in the crystal structure at the perimeter, probability for minority carrier recombination is elevated in this region. Therefore, perimeter recombination is the major recombination loss mechanism in small area MIMs.
- Unique shunting mechanism in studied MIMs is caused by the leakage current flow through semi-insulating substrate between adjacent segments. This effect is especially influential for the device performance at very low irradiance [22] or when the substrate is illuminated by the impinged light [14]; as is the case for the studied device.

The influence of a distinct loss mechanism on the conversion efficiency of the studied device, illuminated with homogeneous monochromatic (λ_0=809 nm) light, is shown in Figure 5. The individual efficiency curves were obtained by individually excluding the distinct loss mechanisms from the model; e.g. for the curve with excluded Joule heating, all resistive components were set to zero. In the following paragraphs, each loss mechanism and its effect on device performance is described and quantified. For more detailed explanations of the presented effects refer to [12].
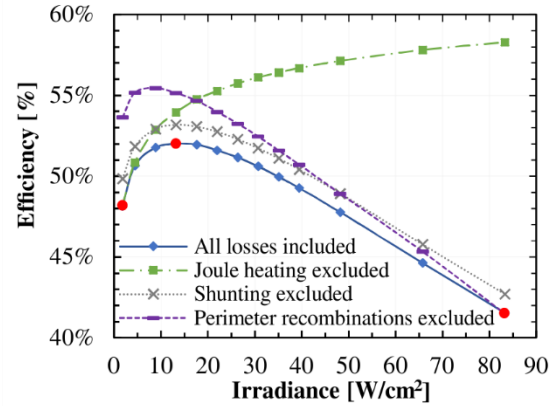
FIGURE 5: The influence of distinct electrical loss mechanism on the monochromatic conversion efficiency (λ_0=809 nm) versus irradiance for the studied six-segment MIM LPC. Red circles on the curve with all losses included mark irradiances for further analysis. Namely: G_{low}=1.8 W/cm^2, $G_{optimal}$=13.2 W/cm^2, G_{high}=83.1 W/cm^2. Modified from [12].

5.1 Joule heating – distributed ohmic losses

Joule heating losses in the studied device increase significantly with increasing irradiance. They are the major cause for impaired device performance at high irradiance. The conversion efficiency is deteriorated by Joule heating by 2%$_{abs.}$ at $G_{optimal}$, but this drop elevates to almost 17%$_{abs.}$ at G_{high}.

The most of the Joule heating is produced by current flow in the lateral conduction layer below the PV segments. This effect accounts for 83%$_{rel.}$ of the overall Joule heating at G_{low} and is further elevated to 88%$_{rel.}$ at G_{high}. Reduction of the LCL sheet resistance to 50% of the current value, would increase conversion efficiency at G_{high} by 6.5%$_{abs.}$

5.2 Recombination losses

Minority carrier recombination losses in the studied device are most severe at low irradiance, as seen in Figure 5. The multi-segment design and small area of the studied device result in a high perimeter to area ratio (P/A=57 cm^{-1}). In combination with GaAs [23, 24] this results in a domination of the perimeter recombination to overall recombination losses for up to very high irradiances. The reason for that is an increased probability for the non-radiative minority carrier recombination at the perimeter, due to either the adsorption of impurities at the perimeter or dangling bonds at the edge of the crystal lattice [24, 25].

To study the effect of perimeter recombination on the efficiency of the device we excluded it from the model by setting J_{02P} to the value of J_{02B}. Conversion efficiency is reduced by 5.5%$_{abs.}$ at G_{low} and by 3.5%$_{abs.}$ at $G_{optimal}$ due to increased recombination at perimeter. Additionally, the peak efficiency of the device without increased perimeter recombination shifts to a lower irradiance (8.8 W/cm^2).

At G_{high} perimeter recombinations become saturated and recombinations in the neutral region determines the recombination losses [12].

Noteworthy, the effect of perimeter recombination can also be clearly observed in the EL images as seen in Figure 4. As discussed above, the pronounced drop in the EL signal is observed all around the perimeter of the *pn*-junctions. Such behavior is expected in small area GaAs PV cells, due to increased non-radiative recombinations in these regions. With proper passivation of the edges of the *pn*-junctions, this loss effect can be mitigated [26]. Therefore, analysis of the spatial EL images can be used to quickly evaluate the performance of the passivation of the GaAs small area cell's edges.

5.3 Shunting losses

The effect of the junction shunting (as present in conventional PV cells) in the studied MIM LPC, is overshadowed by the shunting between adjacent LPC PV segments due to a leakage current through the substrate. We have shown recently, that light impinging on the semi-insulating GaAs substrate at the isolation trenches, causes a significant reduction of the substrate resistivity [14]. This phenomenon leads to a significant leakage current between adjacent segments in the studied device. Due to a reciprocal relationship between the irradiance and the substrate resistivity the conversion efficiency due to this unique phenomenon is impaired by $1.2\%_{abs.}$ independently of irradiance.

6 SUMMARY AND CONCLUSION

In this work we studied the influence of various electrical loss mechanisms (e.g. Joule heating, perimeter minority carrier recombination and shunting through the semi insulating-substrate) on the performance of the small area six-segment monolithically interconnected (MIM) GaAs laser power converter (LPC) based on a distributed 2.5 dimensional model. We paid special attention to the parametrization of the manufactured device, from which we obtained a full set of realistic electrical parameters for the model. Additionally, the complex geometry of the device was preserved in the built model by digital images of the photolithographic masks used in the manufacturing of the device.

Using the model good agreement between measured and simulated illuminated and dark *J-V* curves was achieved. Moreover, the model was independently verified with spatial maps of measured and simulated electroluminescence emission which also showed very good agreement. Thus, the model accurately represents the manufactured device and can be used for analysis of individual electrical loss mechanisms.

Based on the validated model, we studied the influence of the individual electrical loss mechanism on the conversion efficiency of the device, illuminated with various monochromatic (λ_0=809 nm) irradiances. At low irradiance (G_{low}=1.8 W/cm^2), below the peak conversion efficiency, the performance of the device is limited by increased minority carrier recombination at the edges of the *pn*-junction. Here at G_{low}, perimeter recombination accounts for $5.5\%_{abs.}$ decrease in the conversion efficiency. For irradiances above the peak conversion efficiency, Joule heating dominates the losses. At G_{high}=83.1 W/cm^2, conversion efficiency is decreased by $16.8\%_{abs.}$ due to combined ohmic losses. The dominant contribution to Joule heating losses stems from the lateral conduction layer, which accounts for $88\%_{rel.}$ of the overall ohmic losses at G_{high}. Additional $1.2\%_{abs.}$ decrease of conversion efficiency was observed for all irradiances, due to photo-induced leakage current through the semi-insulating GaAs substrate. This effect was identified as a major shunting mechanism in the studied device and completely diminishes the effect of conventional junction shunting.

7 ACKNOWLEDGEMENTS

8 REFERENCES

[1] V. Andreev, V. Khvostikov, V. Kalinovsky, V. Lantratov, V. Grilikhes, V. Rumyantsev, M. Shvarts, V. Fokanov, A. Pavlov, Proceedings of 3rd World Conference on Photovoltaic Energy Conversion (2003) 761–764.

[2] J. Schubert, E. Oliva, F. Dimroth, W. Guter, R. Loeckenhoff, A. W. Bett, IEEE Transactions on Electron Devices 56 (2009) 170–175.

[3] M. York, S. Fafard, Journal of Physics D: Applied Physics 50 (2017) 173003.

[4] R. Pena, C. Algora, I. R. Matías, M. López-Amo, Applied optics 38 (1999) 2463–2466.

[5] G. Bottger, M. Dreschmann, C. Klamouris, M. Hubner, M. Roger, A. W. Bett, T. Kueng, J. Becker, W. Freude, J. Leuthold, IEEE Photonics Technology Letters 20 (2008) 39–41.

[6] K. Worms, C. Klamouris, F. Wegh, L. Meder, D. Volkmer, S. P. Philipps, S. K. Reichmuth, H. Helmers, A. Kunadt, J. Vourvoulakis, A. W. Bett, C. Koos, W. Freude, J. Leuthold, W. Stork, Wind Energy 20 (2017) 345–360.

[7] T. Shan, X. Qi, Infrared Physics & Technology 71 (2015) 144–150.

[8] R. Pena, C. Algora, I. Anton, Proceedings of 3rd IEEE World Conference On Photovoltaic Energy Conversion, Osaka, Japan, Vol.1 (2003) 228–231.

[9] H. Helmers, L. Wagner, C. E. Garza, K. S. Reichmuth, E. Oliva, S. P. Philipps, D. Lackner, A. W. Bett, Proceedings SENSOR 2015, Nürnberg, Germany (2015) 519–524.

[10] E. Oliva, F. Dimroth, A. W. Bett, Prog. Photovolt: Res. Appl. 16 (2008) 289–295.

[11] R. Kimovec, M. Topic, Facta universitatis – series: Electronics and Energetics 30 (2017) 93–106.

[12] R. Kimovec, H. Helmers, A. W. Bett, M. Topič, Submitted for publication (2017).

[13] B. E. Pieters, Proceedings of IEEE 40th Photovoltaic Specialist Conference (PVSC) Denver, CO, USA (2014) 1370–1375.

[14] R. Kimovec, H. Helmers, A. W. Bett, M. Topič, Submitted for publication (2017).

[15] M. Steiner, S. P. Philipps, M. Hermle, A. W. Bett, F. Dimroth, Prog. Photovolt: Res. Appl. 19 (2011) 73–83.

[16] S. K. Reichmuth, H. Helmers, C. E. Garza, D. Vahle, M. de Boer, L. Stevens, M. Mundus, A. W. Bett, G. Siefer, Proceedings of 32nd European Photovoltaic Solar Energy Conference (EU PVSEC), Munich, Germany (2016) 5–10.

[17] D. K. Schroder, Semiconductor Material and Device Characterization, Wiley-IEEE Press, Piscataway, NJ (2006) 1–59.

[18] M. Sotoodeh, A. H. Khalid, A. A. Rezazadeh, Journal of Applied Physics 87 (2000) 2890–2900.

[19] D. C. Look, in Semiconductors and Semimetals, Elsevier (1983) 75–170.

[20] R. Kimovec, H. Helmers, A. W. Bett, M. Topič, Informacije MIDEM – Journal of Microelectronics, Electronic Components and Materials 46 (2016) 142–148.

[21] U. Rau, Phys. Rev. B 76 (2007) 085303.

[22] Y. Wang, N. Chen, X. Zhang, Y. Bai, Y. Wang, T. Huang, H. Zhang, H. Shi, Science China Technological Sciences 53 (2010) 1240.

[23] T. B. Stellwag, P. E. Dodd, M. S. Carpenter, M. S. Lundstrom, R. F. Pierret, M. R. Melloch, E. Yablonovitch, T. J. Gmitter, Proceedings of the 21st IEEE Photovoltaic Specialists Conference, Kissimmee, FL, USA, Vol 1. (1990) 442–447.

[24] P. Espinet-González, I. Rey-Stolle, M. Ochoa, C. Algora, I. García, E. Barrigón, P rog. Photovolt: Res. Appl. 23 (2015) 874–882.

[25] A. Belghachi, S. Khelifi, Solar Energy Materials and Solar Cells 90 (2006) 1–14.

[26] M. T. Sheldon, C. N. Eisler, H. A. Atwater, Advanced Energy Materials 2 (2012) 339–344.